Electric field measurements on plasma bullets in N$_2$ using four-wave mixing

M. van der Schans, P. Böhm, J. Teunissen, S. Nijdam, W. IJzerman and U. Czarnetzki

Electric field measurements on plasma bullets in N_2 using four-wave mixing

Marc van der Schans[1], Patrick Böhm[2], Jannis Teunissen[3,4], Sander Nijdam[1], Wilbert IJzerman[5,6] and Uwe Czarnetzki[2]

[1] Department of Applied Physics, Eindhoven University of Technology, PO Box 513, 5600 MB Eindhoven, The Netherlands

[2] Institute for Experimental Physics V, Ruhr-Universität Bochum, 44780 Bochum, Germany

[3] Centre for Mathematical Plasma-Astrophysics, KU Leuven, Celestijnenlaan 200B, 3001 Leuven, Belgium

[4] Centrum Wiskunde & Informatica (CWI), PO Box 94079, 1090 GB Amsterdam, The Netherlands

[5] Department of Mathematics and Computer Science, Eindhoven University of Technology, PO Box 513, 5600 MB Eindhoven, The Netherlands

[6] Philips Lighting, High Tech Campus 7, 5656 AE Eindhoven, The Netherlands

E-mail: `m.van.der.schans@tue.nl`

Abstract. Atmospheric pressure plasma jets generated by kHz nanosecond voltage pulses typically consist of guided streamer discharges called plasma bullets. In this work, plasma bullets are generated in a pulsed plasma jet using N_2 as feed gas and their electric field distribution is investigated by polarization-resolved four-wave mixing. The method and its analysis have been extended to resolve radial profiles of non-uniform, but radially symmetric, electric field distributions. In addition, a calibration procedure using an electrode geometry different from the discharge geometry has been developed. A radially resolved profile of the axial electric field component of a plasma bullet in N_2 is presented, as well as the temporal development of the (line-integrated) radial and axial components of the electric field. To verify the results they are compared to a streamer model adapted to the conditions of the experiment. The peak values obtained from the experiment are in the range expected from streamer literature. However, there are some quantitative differences with the model, which predicts values approximately a factor two lower than those found in the experiment, as well as a faster radial decay. The temporal development shows similar features in both the experiment and the model. Explanations for these differences are provided and further improvements for the method are outlined.

Keywords: atmospheric pressure plasma jet, plasma bullet, guided streamer, electric field, four-wave mixing, coherent anti-Stokes Raman scattering

Dated: September 8, 2017

1. Introduction

Atmospheric pressure plasma jets have been a topic of high interest in the past few decades for their numerous potential applications in materials processing and biomedicine [1–3]. By now, a wide variety of designs for plasma jet devices utilizing different electrode geometries, feed gas (mixtures) and driving voltages and frequencies exists. As first noted by Teschke *et al* [4] and Lu and Laroussi [5], when AC or pulsed DC voltages in the kHz-range are used, so-called plasma bullets are typically observed in short exposure images of the discharge. These plasma bullets are highly periodic and repeatable streamer-like discharges that all propagate along the same trajectory. The repeatable behavior of plasma bullets is generally ascribed to a memory effect due to remnants of previous discharges [6, 7]. In literature these plasma bullets are sometimes, and perhaps more accurately, referred to as guided ionization waves or guided streamers.

Numerous experimental and numerical investigations have been performed on plasma jets and plasma bullets [7]. In the large majority of these studies a noble gas (He, Ar, Ne or Kr) or a noble gas mixture is used as feed gas, sometimes with small admixtures of molecular species (N$_2$, O$_2$ or H$_2$O). Pure molecular gases or mixtures can also be used, but there are only few studies on plasma jets with N$_2$ or air as feed gas [1]. Nevertheless, plasma bullets have been observed even with air as feed gas [8].

Knowledge on the spatial and temporal distribution of the electric field is essential for both theory and applications, as the electric field drives the discharge and is related to rate coefficients of plasma processes. Still, direct electric field measurements on transient atmospheric pressure discharges have remained challenging. Several recent electric field strength measurements based on the Stark effect in H$_2$ and/or He containing discharges [9–15] and line intensity ratios in He [16] or N$_2$ [17, 18] containing discharges have led to new insights. However, these emission-based methods are limited to the place where and the moment when photons are emitted and they cannot probe the electric field in regions outside the discharge. Another approach is to use the Pockels effect: remote electric field measurements on a plasma jet have been demonstrated using an electro-optic probe [19–21]. In addition, the deposited surface charge and electric field of plasma bullets impinging on a birefringent target have been investigated [22–25]. While such measurements are highly relevant for applications where a target surface is present and the delivered electric field could play an important role, such as in plasma medicine [26], having a target surface present is invasive to the discharge itself.

In this work the electric field of plasma bullets in N$_2$ at atmospheric pressure is investigated by electric field four-wave mixing. This nonlinear laser technique based on coherent Raman scattering can be used to determine the strength of an electric field as well as its direction. The principle of this technique was first mentioned by Gavrilenko *et al* [27]. Basically, two collinear laser beams are used to produce coherent anti-Stokes Raman scattering (CARS) radiation, while simultaneously generating coherent infrared (IR) radiation on a dipole-forbidden molecular Raman transition in the presence of an external electric field. Both processes are examples of four-wave mixing and the intensity

ratio of the resulting CARS and IR radiation is directly related to the electric field. Up to now, this method has primarily been used for electric field measurement in discharges containing H$_2$ [28–37], because of its large Raman cross section. However, it has been shown that N$_2$ can also be used as probe molecule instead [38–41].

When applying electric field four-wave mixing to plasma bullets, a few things need to be considered. Like streamer discharges, plasma bullets are expected to have highly non-uniform electric fields. Because the two laser beams in the experiment are collinear, the IR radiation is produced along some length of the laser path where the electric field of the plasma bullet is not constant. This means that the result of the measurement is actually the line-integrated electric field. To obtain spatially resolved electric field values, the four-wave mixing technique has to be extended with an inversion method. In this work it is shown for the first time that this is feasible. Furthermore, a calibration measurement in a known electric field is required to obtain absolute values from the measurements. The calibration is normally performed by applying a voltage that is below the breakdown value to the discharge electrodes and subsequently measuring the generated CARS and IR beams. However, this is impossible in the present case. The reason is that the plasma bullets propagate into an open atmosphere rather than between two electrodes and as a result the background electric field is too low to calibrate when the applied voltage remains below the breakdown voltage. Therefore, a new calibration procedure using an electrode geometry different from the discharge geometry is also demonstrated. The obtained results are compared to the electric field profiles acquired from a streamer simulation adapted to the conditions of the plasma bullets.

2. Experimental setup and methods

2.1. Discharge setup

In figure 1 the discharge setup is illustrated. Plasma bullets are generated by applying pulsed DC voltages to a needle electrode. The casing of the device that houses the needle electrode is made of polycarbonate and has an inlet for the feed gas on top. In this work N$_2$ (99.999% purity) at a volumetric flow rate of 1 slm (standard liter per minute) is used as feed gas. The feed gas subsequently flows into open air through the nozzle, which is a quartz tube of 1 mm inner radius and 2 mm outer radius. The needle electrode, which is placed concentrically inside the quartz tube, is made of tungsten, has a radius of 0.5 mm and its tip has an angle of approximately 20°. The tip of needle is located 2 mm from the end of the quartz tube. The back of the casing has a high voltage (HV) connector that connects a pulsed power supply to the needle electrode through a brass screw terminal. An additional screw is placed in contact with the screw terminal and is connected to a HV probe (Tektronix P6015A) to monitor the applied voltage. As a grounded electrode is not specified in the setup, the discharge geometry is that of a single electrode plasma jet [1, 2]. A previous version of this plasma source was also used in the research of Hofmann *et al* [6, 42] where plasma bullets in helium and argon were
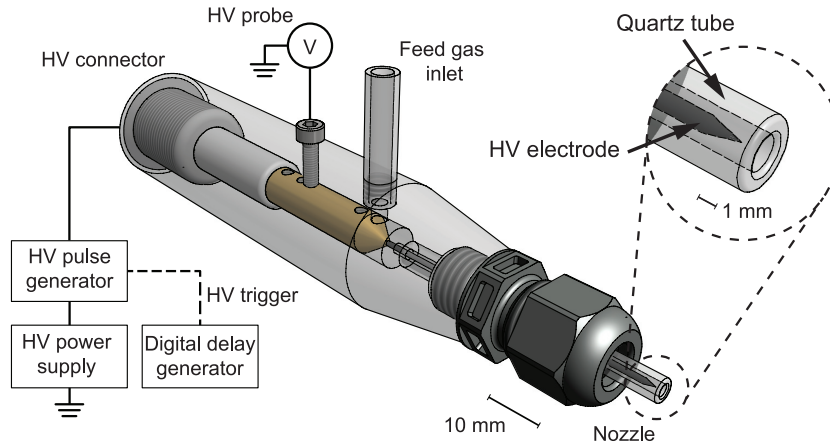
Figure 1. Illustration of the discharge setup including a magnified view of the nozzle and electrode geometry.

investigated.

To generate HV pulses, the output of a DC HV power supply (Spellman UHR10P60) is gated by a HV pulse generator (DEI PVX-4110). The trigger/gate signal for the HV pulse generator is provided by a digital delay generator (Stanford Research Systems DG535), which will also be used to synchronize the discharge to the laser system used for the electric field measurement. For experiments presented in this work a voltage amplitude of 8 kV, a repetition frequency of 3 kHz, and a pulse width of 500 ns are chosen. With this setup voltage rise and fall times of about 40 ns are achieved.

Figure 2 shows a series of images illustrating the propagation of the resulting plasma bullets. Images of the optical emission are recorded using an ICCD camera (Stanford Computer Optics 4 Picos) at several intervals after the inception of the discharge. The discharge closely resembles a traditional streamer discharge in N$_2$, with the maximum emission intensity on the discharge axis. It should be remarked that this is different from the more commonly studied plasma bullets in pure He, where interaction between the discharge and the dielectric tube is often important and typically ring-shaped discharge structures are observed in the emission [7, 43]. From the images the average propagation speed of the bullets is determined to be around 10^5 m/s.

2.2. Electric field four-wave mixing

In the electric field four-wave mixing technique [44, 45] two laser beams are used, a pump laser beam and a Stokes laser beam. The wavelengths of the lasers are chosen such that the difference between the pump beam frequency ω_1 and the Stokes beam frequency ω_2 matches a dipole-forbidden vibrational Raman transition of the probe molecule. In this case the transition is the Q-branch of N$_2$ in the electronic ground state, which corresponds to a wavenumber of 2331 cm^{-1} or a wavelength of 4.3 µm [38]. At sufficiently high laser intensities this will lead to two third-order nonlinear optical interactions between the lasers and the present N$_2$ molecules. Firstly, coherent anti-Stokes Raman scattering
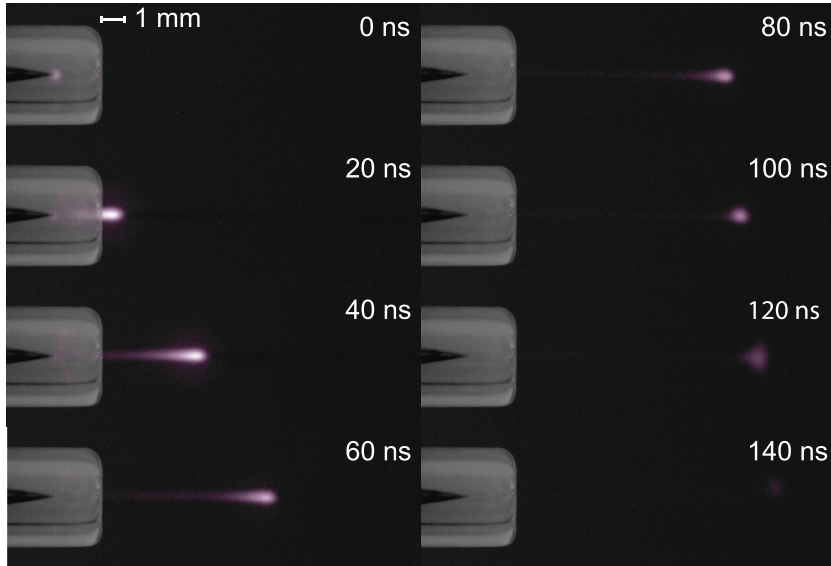
Figure 2. Composed images illustrating the propagation of the plasma bullets. For each of the images 500 exposures are collected with a gate time of 1 ns. The background of the image showing the nozzle as well as the colors were added in post-processing for illustrational purposes.
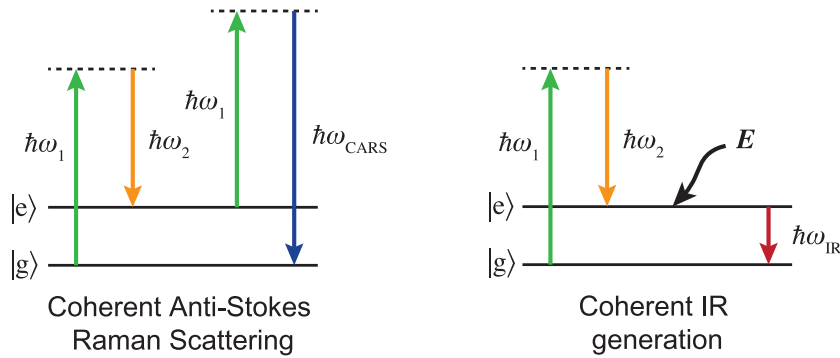

Figure 3. Energy diagrams for the two four-wave maxing processes. The dashed lines indicate virtual levels.

(CARS) will occur. In this interaction photons with a frequency $\omega_{\mathrm{CARS}} = 2\omega_1 - \omega_2$ that is anti-Stokes shifted from the pump frequency ω_1 are generated coherently in a laser-like beam. When an external electric field $\boldsymbol{E}$ is present a second four-wave mixing process, similar to CARS, will occur simultaneously. In this process IR photons with frequency $\omega_{\mathrm{IR}} = \omega_1 - \omega_2$ are coherently generated on the Raman transition in a laser-like beam. Energy diagrams for both CARS and coherent IR generation are shown in figure 3, where $|\mathrm{g}\rangle$ and $|\mathrm{e}\rangle$ indicate the ground state and vibrationally excited state respectively. It should be noted that both processes are single parametric events and hence do not result in population of the excited state.

From nonlinear optics the following equations can be derived for the amplitudes

A_{CARS} and A_{IR} of the CARS and IR signals in the plane-wave approximation [46]:

$$\frac{\mathrm{d}}{\mathrm{d}x}A_{\text{CARS}} \propto \chi^{(3)}(\omega_{\text{CARS}})A_1{}^2 A_2^* \exp(-i\Delta kx), \tag{1}$$

$$\frac{\mathrm{d}}{\mathrm{d}x}A_{\text{IR}} \quad \propto \chi^{(3)}(\omega_{\text{IR}})A_1 A_2^* E \exp(-i\Delta k'x), \tag{2}$$

where $\chi^{(3)}(\omega)$ is the third-order nonlinear susceptibility corresponding to the interaction, A_1 and A_2 are the amplitudes of the incident pump and Stokes beams, and $\Delta k = k_{\text{CARS}} - 2k_1 + k_2$ and $\Delta k' = k_{\text{IR}} - k_1 + k_2$ are wavevector mismatches. The fields are generated most efficiently under perfect phase matching conditions, $\Delta k = \Delta k' = 0$. In a conventional CARS experiment phase matching can be achieved with crossed laser beams, which is called the BOXCARS configuration [45]. Local measurements with high spatial resolution can be achieved this way, because the CARS beam is only generated in the small region where the laser beams cross. However, for the coherent IR generation process phase matching is only achieved when the pump and Stokes beams are collinear, and therefore a collinear laser beam configuration has to be used.

The wavevector mismatch in this configuration can be estimated as $\Delta k' = (n_{\text{IR}}\omega_{\text{IR}} - n_1\omega_1 + n_2\omega_2)/c \approx -0.2\,\text{cm}^{-1}$, where n is the refractive index at each of the frequencies and c is the vacuum speed of light. This corresponds to a coherence length of the process, $L_{\text{IR}}^{\text{coh}} = \pi/|\Delta k'|$, of the order of $10\,\text{cm}$. The spatial extent of the studied electric fields in the direction of the laser beams will typically only be around a centimeter and shorter, hence the maximum phase mismatch is only about $|\Delta k'x| = 0.2$. Since $0.2 < \pi$, this indicates that each part of the electric field distribution will contribute constructively to A_{IR}. (Note that this is equivalent to stating that the spatial extent of the electric field is shorter than $L_{\text{IR}}^{\text{coh}}$). Furthermore, the factor by which the final IR amplitude is multiplied due to the mismatch, compared to the perfectly phase matched case, can be estimated by $\text{sinc}(\Delta k'x/2)$ [46], which results in 0.998. So the impact of the mismatch can be expected to be less than 1% in this case and it is therefore neglected.

With both incident laser beams propagating along the x-axis and neglecting the phase matching exponents, (1) and (2) are now integrated, which results in

$$A_{\text{CARS}} \propto \chi^{(3)}(\omega_{\text{CARS}})A_1{}^2 A_2^* L_{\text{CARS}}, \tag{3}$$

$$A_{\text{IR}} \quad \propto \chi^{(3)}(\omega_{\text{IR}})A_1 A_2^* \int_{-\frac{1}{2}L_{\text{IR}}}^{\frac{1}{2}L_{\text{IR}}} E\,\mathrm{d}x, \tag{4}$$

where L_{CARS} and L_{IR} are the 'interaction lengths', the regions along the laser beams that can contribute to the generated signals. In practice focused laser beams are used and the interaction length is typically multiple Rayleigh lengths around the focus spot (which is here chosen at $x = 0$) [47]. In fact, in a recent study by Simeni Simeni *et al* the response of the IR beam was measured as a function of distance from the focus spot. It showed that regions more than $10\,\text{cm}$ from the focus spot can still generate an IR signal [41]. However, in the present case the electric field to be measured should ideally be contained in a region well within the Rayleigh range from each side of the focus point. In this way, the only contribution to the IR beam comes from the part of the interaction length where the plane-wave approximation holds, and hence 4 is valid. This fact is

actually also reflected in the measured IR response in [41]: while the IR beam can still be generated at locations more than $10\,\mathrm{cm}$ away from the focus spot, the response is flat in a range of only several centimeter around the focus spot. Additionally, in more extended electric field distributions the phase matching that was neglected in (4) should also be considered.

Now the intensities, $I \propto AA^*$, of the CARS and IR beams are given by

$$I_{\mathrm{CARS}} \propto |\chi^{(3)}(\omega_{\mathrm{CARS}})|^2 I_1{}^2 I_2 L_{\mathrm{CARS}}^2, \tag{5}$$

$$I_{\mathrm{IR}} \quad \propto |\chi^{(3)}(\omega_{\mathrm{IR}})|^2 I_1 I_2 \left(\int_{-\frac{1}{2}L_{\mathrm{IR}}}^{\frac{1}{2}L_{\mathrm{IR}}} E\,\mathrm{d}x \right)^2, \tag{6}$$

where I_1 and I_2 are the intensities of the incident pump and Stokes laser beams respectively. Finally, (5) and (6) can be combined to obtain

$$\left| \int_{-\frac{1}{2}L_{\mathrm{IR}}}^{\frac{1}{2}L_{\mathrm{IR}}} E\,\mathrm{d}x \right| = C_{\mathrm{cal}} \sqrt{I_1 \frac{I_{\mathrm{IR}}}{I_{\mathrm{CARS}}}}, \tag{7}$$

where C_{cal} is a constant that can be determined from a calibration measurement in a known electric field. In the case of a constant electric field, (7) can be reduced to $|E| = C_{\mathrm{cal}}\sqrt{I_1 I_{\mathrm{IR}} I_{\mathrm{CARS}}^{-1}}$ (here L_{IR} is absorbed into C_{cal}). This is the form that is used in [28–41]. It should be realized however that the result is an average value of the field strength when this equation is used in a non-uniform electric field.

Up to now it has been implicitly assumed, through the scalar nature of (2), that the polarization direction of the lasers and the direction of the electric field are all parallel to each other. This is however not necessary and actually the direction of the electric field, apart from its sign, can be determined by considering the polarization of the IR beam. When the lasers are polarized parallel to each other, say in the z-direction, it can be shown that [44]

$$I_{\mathrm{IR}}^{(z)} \propto |\chi_{zzzz}^{(3)}(\omega_{\mathrm{IR}})|^2 I_1 I_2 \left(\int_{-\frac{1}{2}L_{\mathrm{IR}}}^{\frac{1}{2}L_{\mathrm{IR}}} E_z\,\mathrm{d}x \right)^2, \tag{8}$$

$$I_{\mathrm{IR}}^{(y)} \propto |\chi_{yyzz}^{(3)}(\omega_{\mathrm{IR}})|^2 I_1 I_2 \left(\int_{-\frac{1}{2}L_{\mathrm{IR}}}^{\frac{1}{2}L_{\mathrm{IR}}} E_y\,\mathrm{d}x \right)^2, \tag{9}$$

where the superscript on I_{IR} indicates which polarization component of the IR beam is measured. The subscripts on the corresponding elements of the susceptibility tensor indicate from left to right the polarization (component) of: the IR beam, the electric field, the pump beam and the Stokes beam. Thus, by measuring the IR intensity polarization-resolved, parallel and perpendicular to the laser polarization, two orthogonal components of the electric field can be determined separately. Combining (8) and (9) with (5) gives

$$\left| \int_{-\frac{1}{2}L_{\mathrm{IR}}}^{\frac{1}{2}L_{\mathrm{IR}}} E_z\,\mathrm{d}x \right| = C_{\mathrm{cal}}^{(z)} \sqrt{I_1 \frac{I_{\mathrm{IR}}^{(z)}}{I_{\mathrm{CARS}}}}, \tag{10}$$

$$\left| \int_{-\frac{1}{2}L_{\mathrm{IR}}}^{\frac{1}{2}L_{\mathrm{IR}}} E_y\,\mathrm{d}x \right| = C_{\mathrm{cal}}^{(y)} \sqrt{I_1 \frac{I_{\mathrm{IR}}^{(y)}}{I_{\mathrm{CARS}}}}, \tag{11}$$
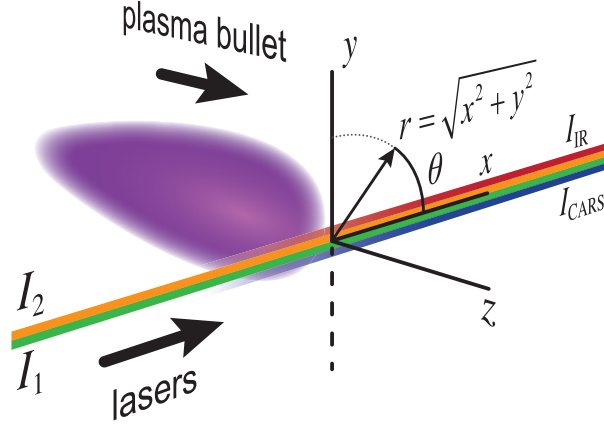
Figure 4. Illustration of the generated CARS and coherent IR beams in the electric field in front of the plasma bullet.

where $C_{\text{cal}}^{(z)}$ and $C_{\text{cal}}^{(y)}$ are again calibration constants, which can be determined from measuring the intensities in a known electric field distribution. These are the equations in the form that will be used in this work to measure the electric field distribution of plasma bullets.

As a side note, it can be seen from (8) and (9) that the IR polarization is parallel to the electric field if the electric field is either parallel or perpendicular to the laser polarization. However, since $\chi_{zzzz}^{(3)} = \chi_{yyzz}^{(3)} + \chi_{yzyz}^{(3)} + \chi_{yzzy}^{(3)}$ [46], there can be an angle of up to 6° for the case of N_2 between the IR polarization and the electric field when the electric field is neither parallel nor perpendicular to the laser polarization [47].

The plasma bullet, incident laser beams and the generation of the CARS and IR beams are illustrated in figure 4. A coordinate system is chosen such that the bullet propagates along the z-axis in the positive direction and the laser beams travel parallel to the x-axis in the positive direction and are linearly polarized in the z-direction. It is assumed that the electric field $\boldsymbol{E}$ of the plasma bullet is radially symmetric:

$$\boldsymbol{E}(r, z, t) = E_r(r, z, t)\hat{\mathbf{e}}_{\mathbf{r}} + E_z(r, z, t)\hat{\mathbf{e}}_{\mathbf{z}}. \tag{12}$$

The electric field component perpendicular to the laser propagation direction, $\boldsymbol{E}_\perp$, consists of the y-component and the z-component and is given by

$$\boldsymbol{E}_\perp(r, \theta, z, t) = E_y(r, \theta, z, t)\hat{\mathbf{e}}_{\mathbf{y}} \quad + E_z(r, z, t)\hat{\mathbf{e}}_{\mathbf{z}} \tag{13}$$

$$= E_r(r, z, t)\sin\theta\hat{\mathbf{e}}_{\mathbf{y}} + E_z(r, z, t)\hat{\mathbf{e}}_{\mathbf{z}}. \tag{14}$$

When the incident laser beams are at a position (y, z), the equations for each of the polarization components can be written as

$$\left| \int_{-\frac{1}{2}L_{\text{IR}}}^{\frac{1}{2}L_{\text{IR}}} E_z(r, z, t)\,\mathrm{d}x \right| = C_{\text{cal}}^{(z)}\sqrt{I_1 \frac{I_{\text{IR}}^{(z)}(y, z, t)}{I_{\text{CARS}}}}, \tag{15}$$

$$\left| \int_{-\frac{1}{2}L_{\text{IR}}}^{\frac{1}{2}L_{\text{IR}}} E_r(r, z, t)\sin\theta\,\mathrm{d}x \right| = C_{\text{cal}}^{(y)}\sqrt{I_1 \frac{I_{\text{IR}}^{(y)}(y, z, t)}{I_{\text{CARS}}}}. \tag{16}$$

To obtain E_z and E_r, except for their signs, an inversion has to be applied. Since $E_z(r, z, t)$ is radially symmetric, (15) has the form of an Abel transform [48] and hence $|E_z(r, z_0, t_0)|$ can be obtained for an axial position $z = z_0$ and time $t = t_0$ by determining the right hand side of (15) as a function of y and subsequently performing an Abel inversion. The integrand of (16), $E_r(r, z, t) \sin \theta$, is however not radially symmetric because of $\sin \theta$ factor, and an Abel inversion cannot be applied. Although not attempted in this work, it should in principle be possible to adjust a (Fourier) series expansion algorithm for Abel inversion, such as those described in [49, 50], to include this factor in the calculation and perform the inversion. Finally, it must be noted that these inversions result in radially resolved profiles but the resulting spatial and temporal resolution still depend on the measurement system.

2.3. Laser setup and calibration

The laser system used for the experiments is mostly the same as the one described in [36], with only the wavelengths adapted for the vibrational Raman transition of N_2 instead of H_2. Furthermore, an additional polarizer was placed in front of the IR detector to measure $I_{IR}^{(z)}$ and $I_{IR}^{(y)}$ separately. A schematic representation of the setup is shown in figure 5.

Two 20 Hz ns-pulsed lasers are used to generate the pump (I_1) and Stokes (I_2) beams for the four-wave mixing experiment. The main laser is a frequency doubled Nd:YAG laser (Continuum Powerlite Precision II 9020) that produces 6.0 ns FWHM pulses with a pulse energy of 650 mJ and $\lambda_1 = 532$ nm. Part of its output (approximately 10%) is used as the pump beam in the experiment and the other part (approximately 90%) is used to pump a dye laser (Radiant Dyes Jaguar D90MA). A mix of Rhodamine B and Rhodamine 101 dyes dissolved in ethanol is used to produce the Stokes beam, which consists of 4.3 ns FWHM pulses with a pulse energy of 47 mJ and $\lambda_2 = 607$ nm.

Both laser beams are focused collinearly in front of the nozzle of the discharge setup by a $f = 300$ mm lens. The generated CARS and IR beams are collected by a second lens and dispersed by a set of prisms. The first prism separates the IR beam, which is subsequently focused onto a HgCdTe IR detector (Vigo System PVI-3 TE-4). A polarizer is placed in front of the IR detector to measure each of the polarization components of the IR beam, and hence each of the components of the electric field, individually. The laser beams and the CARS beam pass through another prism, after which the laser beams are directed into a beam dump and the CARS beam intensity is measured by photodiode 1. To monitor the intensity of the pump laser, a higher order reflection of the pump beam from the first prism is measured by photodiode 2.

A frequency divider paired with two digital delay generators (Stanford Research Systems DG535) is used to generate synchronized 20 Hz and 3 kHz signals to trigger the laser system and HV pulser respectively. By adjusting the delay between the laser trigger and HV trigger the electric field can be measured at different times during the propagation of the plasma bullet. Furthermore, the plasma source itself is mounted
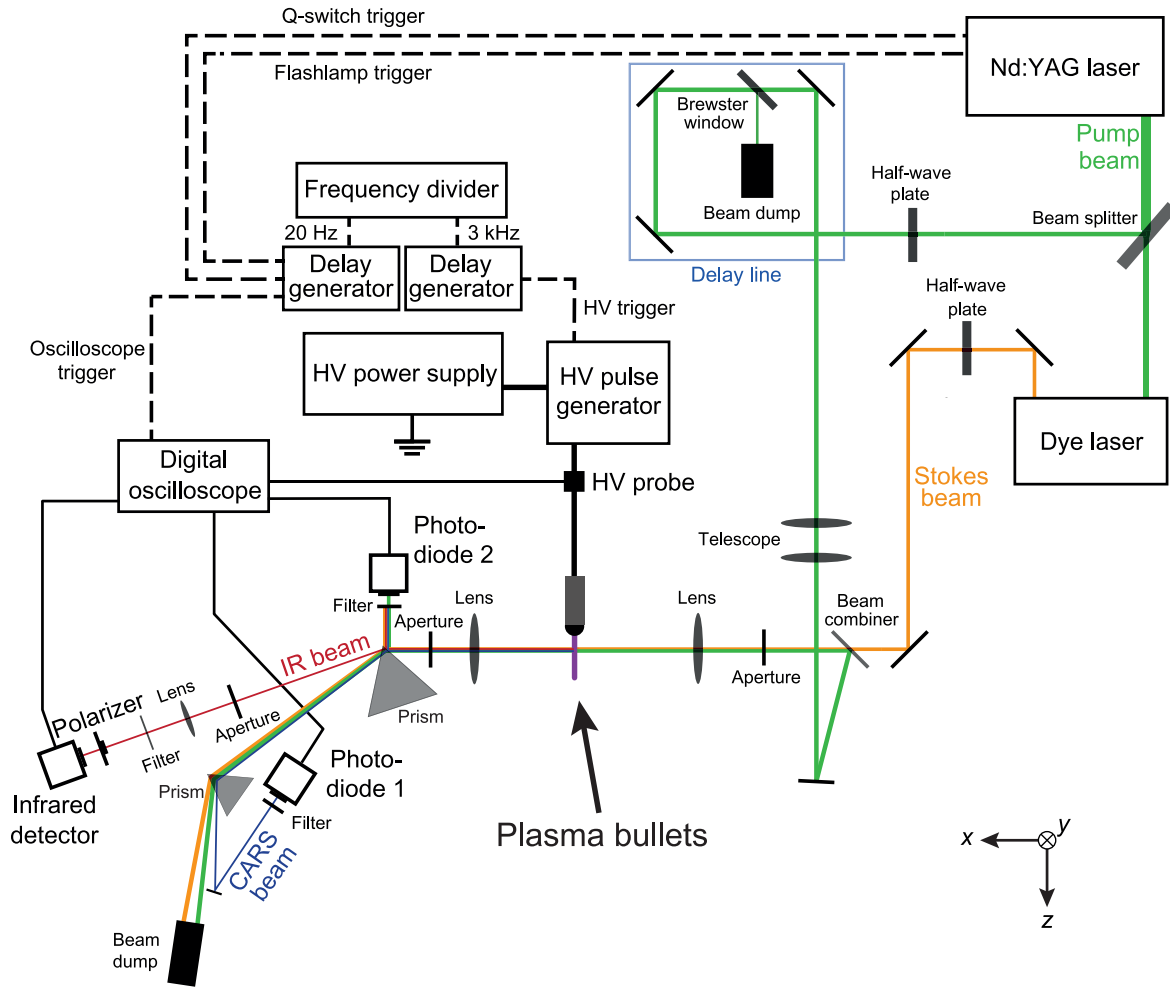
Figure 5. Schematic drawing of the experimental setup used for the electric field measurements.

on a three-axis motorized stage (Zaber Technologies T-XYZ-LSM050A) to probe the electric field at different positions. Therefore this setup allows for the determination of the spatial and temporal development of the electric field and its polarization direction.

The achievable resolution of the system is largely determined by the properties of the focused laser beams, which are summarized in table 1. Since both laser beams need to be present, the spatial and temporal resolution is approximated by the smallest waist diameter and shortest pulse duration respectively. This means that the spatial resolution is about $100\,\mu\mathrm{m}$. However, the temporal resolution of about $4.3\,\mathrm{ns}$ limits the axial resolution, because at an average propagation speed of about $10^5\,\mathrm{ms}^{-1}$, the plasma bullet advances about $500\,\mu\mathrm{m}$ during the duration of the laser pulse. So the spatial resolution for the electric field measurements on plasma bullets is estimated at $100\,\mu\mathrm{m}$ laterally and $500\,\mu\mathrm{m}$ axially.

When a discharge takes place between two electrodes the setup can normally be calibrated in-situ or at least using the discharge electrodes themselves, because the background fields produced by voltages below the breakdown value are sufficiently large.

Table 1. Properties of the focused laser beams.

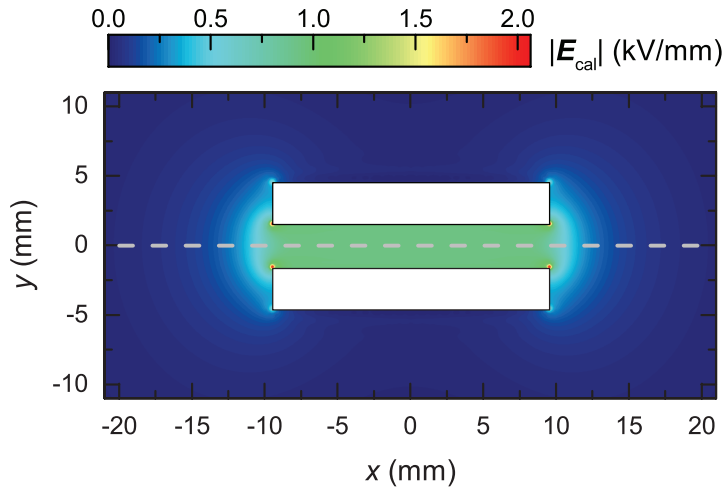| Laser	Waist (µm)	Rayleigh length (mm)	Pulse duration (ns)
Nd:YAG	98	14	6.0
dye	135	24	4.3

Figure 6. Center part of the electric field distribution of the calibration geometry when 3 kV is applied. The white rectangles indicate the position of the electrodes and the dashed grey line shows a part of the path along which the electric field is integrated. The full domain of the model is 260 mm wide and 40 mm high.

For the currently used single electrode plasma jet this is, however, not the case and therefore an alternative ex-situ absolute calibration procedure is implemented. Equations (8) and (9) show that $C_{\mathrm{cal}}^{(z)}$ and $C_{\mathrm{cal}}^{(y)}$ can actually be obtained from any electrode geometry as long as the electric field distribution is known and the integral on the left hand side can be calculated. To this end, two square 19 mm × 19 mm parallel plate electrodes with a gap of 3.1 mm are used. The center of the gap is placed at the same point along the beam path where the actual measurements take place. The size of 19 mm was chosen such that the calibration electric field is situated well within the shortest Rayleigh range from each side of the focus spot ($2 \times 14\,\mathrm{mm} = 28\,\mathrm{mm}$). In addition, the electrodes can be rotated around the laser beam path such that the calibration field is oriented in either the z- or y-direction. The resulting electric field distribution is obtained from an electrostatic model in COMSOL and subsequently the integral along the laser path is calculated. An example is shown in figure 6. The full domain of the electrostatic model is 260 mm by 40 mm to make sure the entire calibration field is accounted for in the integral.

2.4. Discharge simulation model

To compare results from the four-wave mixing experiment to simulations, an axisymmetric fluid model was adjusted to the experimental conditions. The model is of the drift-

diffusion type in combination with the local field approximation [51], so that the electron density n_e and ion density n_i evolve in time as:

$$\frac{\partial}{\partial t} n_e = \nabla \cdot (\mu_e \boldsymbol{E} n_e + D_e \nabla n_e) + \alpha \mu_e E n_e, \tag{17}$$

$$\frac{\partial}{\partial t} n_i = \alpha \mu_e E n_e, \tag{18}$$

where μ_e, D_e and α are the electric field dependent electron mobility, diffusion and ionization coefficients respectively. The electric potential ϕ is calculated using Poisson's equation

$$\nabla^2 \phi = -\frac{e(n_i - n_e)}{\varepsilon_0}, \tag{19}$$

where e is the elementary charge and ε_0 is the vacuum permittivity, and the electric field is given by $\boldsymbol{E} = -\nabla \phi$. The transport coefficients for N_2 (at $1\,\text{bar}$ and $293\,\text{K}$) were computed from the Phelps database [52] using Bolsig+ [53]. Note that the model assumes that ions are immobile, and that the discharges propagate in N_2 and therefore photoionization is not included. The above equations are solved on an adaptively refined mesh using the Afivo framework [54], which was used before in [55].

A computational domain with a radius and height of $10\,\text{cm}$ was used, mimicking the typical dimensions of the experiment. However, precisely reproducing the experiment's electrode geometry was not possible: the electrode and the surrounding dielectrics cannot easily be included in our numerical model, and the experiments are performed in open space without a clear reference point for the boundary conditions for the potential. Therefore, to simulate the electrode as well as possible in this situation, it is approximated by an ionized channel protruding $1.5\,\text{cm}$ into the domain. The resulting potential of this artificial electrode is illustrated in figure 7a. The channel representing the electrode has a charged particle density of $n_e = n_i = 10^{14}\,\text{cm}^{-3}$ and a radius of $0.5\,\text{mm}$, which is reduced to $0.25\,\text{mm}$ at its tip. The decrease in radius and electric field at the tip of the channel is shown in figure 7b. As the electrons electrically screen the channel, it acts approximately as a conducting electrode. On the top boundary of the domain a potential of $8\,\text{kV}$ is applied, which radially decays as $\log(1 + d_0/r)$, with $d_0 = 10\,\text{cm}$. The bottom boundary is electrically grounded and a Neumann zero boundary condition is used at the radial boundary.

The background preionization due to previous pulses (the memory effect) is included as a gaussian profile of electrons and ions. The profile has a characteristic width of $0.25\,\text{mm}$, assuming the previous discharges had a radius approximately equal to the emission HWHM of about $0.15\,\text{mm}$, and that the typical diffusion length $\sqrt{4Dt}$ between pulses at $3\,\text{kHz}$ is about $0.1\,\text{mm}$. The maximum density of the preionization at the start of a new discharge was estimated to be $10^9\,\text{cm}^{-3}$ from a zero dimensional model presented in [56].

Figure 8 shows the time evolution of the simulated discharge. Between 10 and $20\,\text{ns}$ the streamer has a velocity of approximately $2 \times 10^5\,\text{m/s}$, in good agreement with the experimental measurement of $1.8 \times 10^5\,\text{m/s}$ in the same time interval. In the simulations,
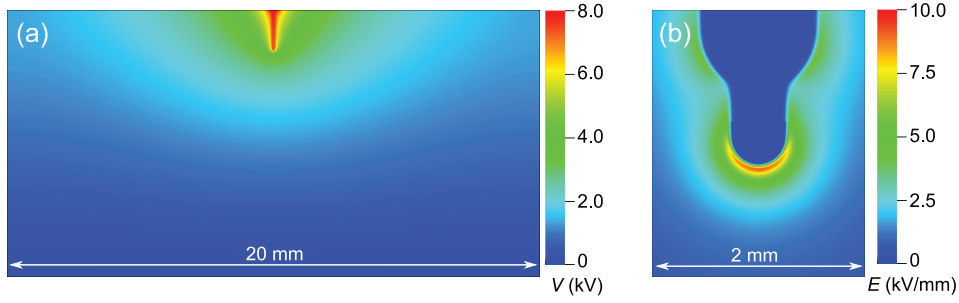
Figure 7. Cross section of the electric potential in the domain, illustrating the artificial electrode represented by an ionized channel (a), and a magnified view of the tip of the channel and the resulting electric field (b).
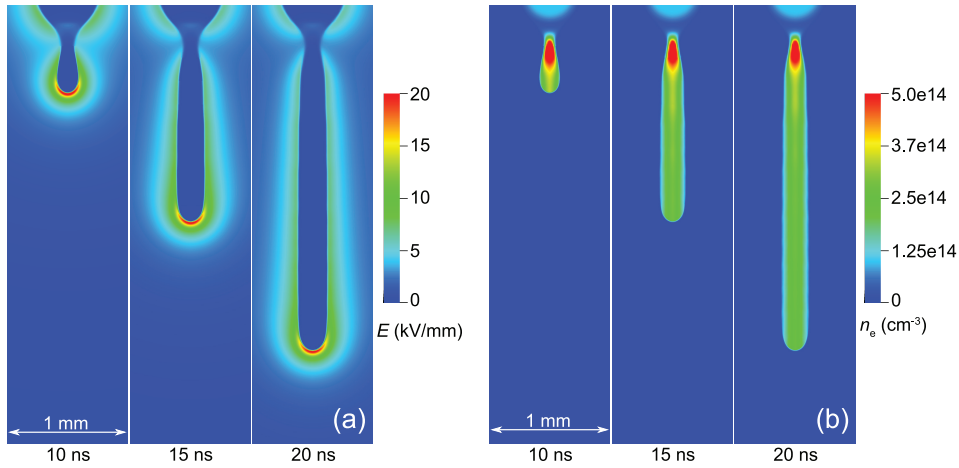

Figure 8. Cross sections showing the simulated electric field (a) and electron density (b) at 10, 15 and 20 ns. The streamer's velocity is about 2×10^5 m/s during the shown interval.

the streamer's diameter ($0.2 \, \text{mm}$), maximum electric field ($20 \, \text{kV/mm}$) and its degree of ionization ($3 \times 10^{14} \, \text{cm}^{-3}$) show little variation between 10 and 20 ns.

Although our numerical model does not calculate the excited species and their emission, it is interesting to consider the ionization source term, $\alpha \mu_e E n_e$, and use this to qualitatively approximate the emission profile. To do so, it is assumed that the number of excited states produced is proportional to the ionization source term and that the decay of emitting states is dominated by collisional quenching. Furthermore, assuming that most of the emission is from the second positive system (SPS) of N_2 results in an effective radiative lifetime that is equal to the quenching time $\tau_q = 2 \, \text{ns}$ [57, 58]. The "emission" is computed from the equation $\partial_t I = -I/\tau_q + \alpha \mu_e E n_e$, and subsequently an Abel transform is applied to obtain a line-of-sight integrated profile. Figure 9 shows both the ionization source term and the approximated emission profile. While the emission profiles indeed resemble the bullet-like shapes observed in the emission shown in figure 2, it should be realized that the ionization is concentrated in a thin region in front of the streamer.
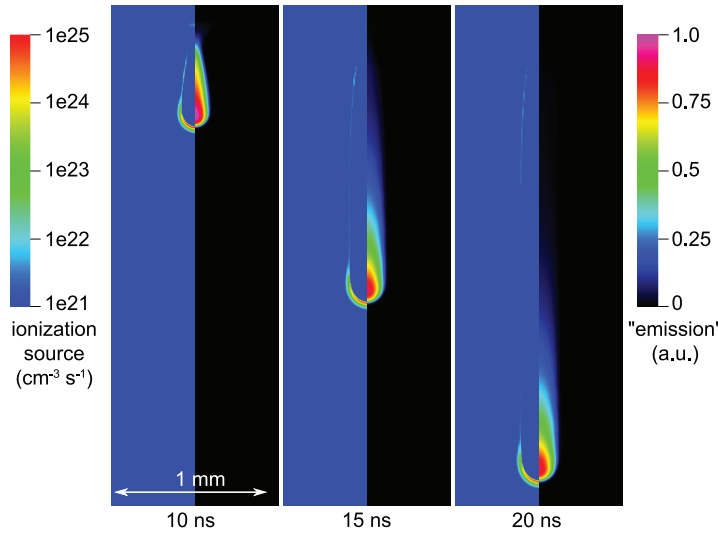
Figure 9. Cross sections showing the ionization source term on the left, and a qualitative approximation of the line-of-sight integrated emission profile (see text) on the right, at 10, 15 and 20 ns.

3. Results and discussion

3.1. Calibration measurement

First the calibration electrodes are placed in the setup, such that the calibration field in the gap is parallel to the electric field component to be measured, and a calibration measurement is performed as described earlier. The intensities measured for a range of applied voltages and their corresponding calculated electric field integrals are plotted in figure 10. As expected from (10) and (11), a linear relation between the electric field integrals and the square root of the intensities is found. Now $C_{\mathrm{cal}}^{(z)}$ and $C_{\mathrm{cal}}^{(y)}$ are given by the reciprocal of the slope of a linear fit from a measurement with the calibration field in the z- and y-direction respectively. Since the laser system has a certain pointing stability, this procedure is repeated before every measurement series to account for changes in the spatial overlap of the two laser beams between measurement series. Furthermore, the threshold value of the electric field integral for which the IR intensity surpasses the noise level of the IR detector also depends on how well the laser beams are aligned. It is found that this usually leads to a threshold value around $|\int E\,\mathrm{d}x| \approx 4\,\mathrm{kV}$.

3.2. Plasma bullet measurements

The results of two types of experiments are presented in this subsection. The first is a spatial scan made in the y-direction by moving the plasma source using the motorized stages, at a fixed distance from the nozzle, at a fixed time after the bullet's inception, to determine the radial distribution of the electric field. The second is a temporal scan, made by changing the delay between the HV trigger and the laser trigger, performed at three fixed y-positions to determine the evolution of the electric field integrals as the
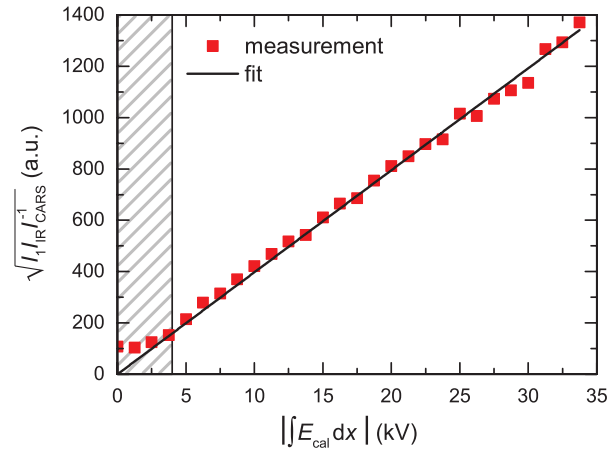
Figure 10. Example of a calibration measurement. The hatched area indicates the region that is below the measurement threshold.
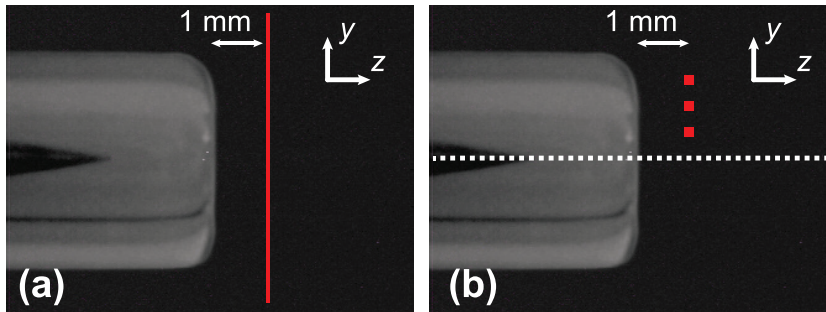

Figure 11. Illustration of the measurement positions. The spatial scan is performed along the red line shown in (a). The temporal scans are performed at the fixed y-positions indicated by the red points in (b). The white dotted line indicates the axis of the jet.

plasma bullet propagates. In each case, both the y- and z-components of the electric field are measured separately by rotating the transmission axis of the polarizer in front of the IR detector accordingly.

3.2.1. Spatial scan and radial distribution The spatial scan in the y-direction is performed at a fixed distance from the nozzle $z_0 = 1\,\mathrm{mm}$ (and hence $3\,\mathrm{mm}$ from the needle tip) at a fixed time after the bullet's inception t_0. The red line in figure 11a shows the measurement positions of this experiment. The fixed timing t_0, which is controlled by the delay between the HV trigger and laser trigger, for this measurement set was chosen such that the highest signal from the IR detector was obtained. This timing corresponds to the situation where the plasma bullet reaches the laser beam path during the measurement, as confirmed by ICCD camera images. Figure 12 shows the integrated electric field values for each of the components. The measurements were performed with $0.5\,\mathrm{\mu m}$ intervals in the y-direction and then collected in $200\,\mathrm{\mu m}$ wide bins, so each of the points in figure 12 contains the data of 400 individual laser shots. The z-component of
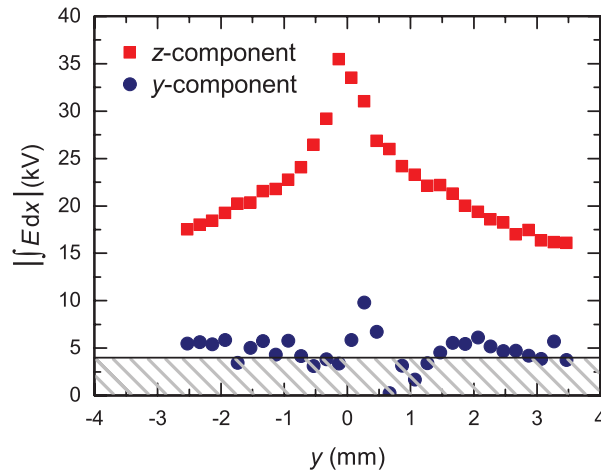
Figure 12. Measured radial profiles of the line integrated electric field components. The hatched area indicates the region that is below the measurement threshold.

the electric field, which is in the propagation direction of the plasma bullet, shows a clear peak at the jet axis. Several millimeters from the jet axis the measured z-component integrals are still significantly above the measurement threshold value. As expected, the y-component is significantly lower than the z-component. In fact, all the measurements of the y-component are around the threshold value and only the z-component is further analyzed.

In order to obtain $|E_z(r, z_0, t_0)|$, the z-component data has to be Abel inverted. For the inversion it is however necessary to know how the distribution decreases to zero. Since the measurements do not reach zero in the probed range, a function is first fitted to the data. Because the shape of the chosen function will influence the peak value and the radial decay of the inverted profiles, two fit functions that fit the data reasonably well are used: one that decreases rapidly and one that decreases slowly to zero. The actual shape is expected to be somewhere in between. Fit 1 is the sum of a gaussian function and a lorentzian function and fit 2 is the convolution of a generalized normal function, i.e. $f(y; a, b, c) = a \exp(-|y|^c/b)$, and a gaussian function. The data and these fits are shown together in figure 13. The fits are subsequently Abel inverted and the obtained electric field profiles are shown in figure 14.

The obtained electric field profile has a peak value of about 12–18 kV/mm and a full width at half maximum (FWHM) of about 750–900 µm. The found peak value is in the same range of about $10\,\mathrm{kV/mm}$ to $35\,\mathrm{kV/mm}$ as the values reported for other streamer discharges in N_2 and N_2-O_2 mixtures [59–61]. It should however be noted that the experimental value found in this work underestimates the peak value, due to the limited spatial resolution in the axial direction resulting from the propagation of the bullet during the laser pulse.

These experimental results will now be compared with the results from the streamer model discussed in section 2.4. In order to do so, the axial (z) component of the electric field is calculated from the simulation data. Subsequently, the electric field is spatially
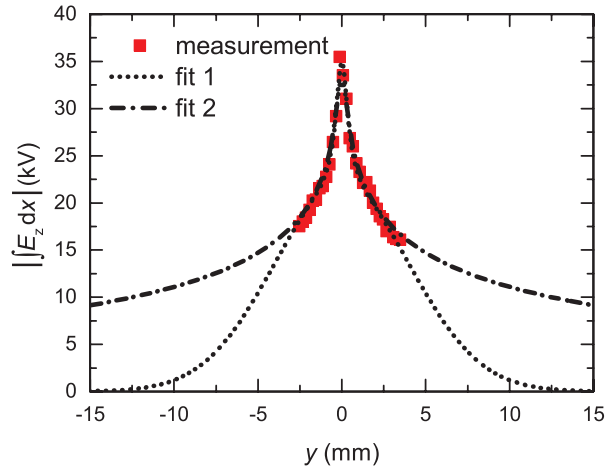
Figure 13. Radial profile of the line integrated z-component values together with the two fits.
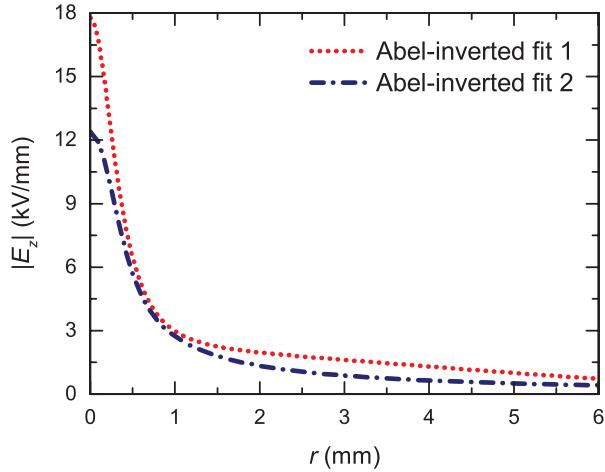

Figure 14. Radial profile of the z-component of the electric field.

and temporally convolved with the profiles of the laser beams. Finally, the resulting radial profile at the timing and position equivalent to the measurement, i.e. 3 mm from the artificial electrode, is convolved with a 200 μm wide rectangular function to mimic the effect of the binning. The obtained peak value after convolution is about 7 kV/mm, which is approximately a factor 2.5 lower than the peak value of about 20 kV/mm before convolution, as visible in figure 8. This is mostly due to the convolution with the temporal beam profile.

A comparison between the experiments and the model (after convolution) in absolute values is shown in figure 15a. It can be seen that the model predicts lower electric field values. The peak value is about a factor 2 lower than the value from the experiment. From the comparison of the normalized profiles in figure 15b it is also apparent that the model predicts a faster radial decay, with a FWHM of approximately 350 μm.

From the modeling point of view, several factors could contribute to these differences. In general, the approximations used for the plasma fluid model could cause differences
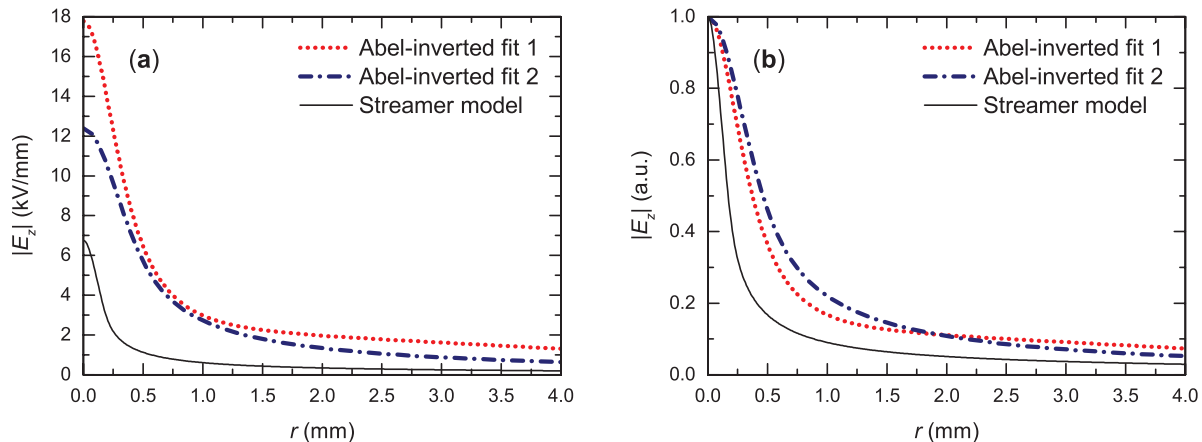
Figure 15. Comparison between the results obtained from the experiment and the model convolved with the laser beam profiles in absolute values (a) and normalized (b).

of perhaps 10–30% in quantities such as the maximum electric field. The model could also only approximate the experimental electrode geometry: it uses a preionized channel instead of an electrode, it does not contain dielectric material around it, and there is also uncertainty in the boundary conditions for the electric potential. The amount of background ionization from previous pulses mimicking the memory effect was roughly estimated, and could easily be an order of magnitude higher or lower. The radial decay of the background ionization could be inaccurate as well. Lastly, the background ionization was included as electrons and positive ions in the model, whereas realistically there are many species.

In previous numerical studies on plasma bullets in He, Boeuf *et al* found that the on-axis electric field at the streamer front increased by only a factor of 1.3 when the preionization density was decreased by four orders of magnitude [62], and Breden *et al* found that the electrode geometry mostly affects the breakdown and propagation inside the nozzle, while the streamer structure outside the nozzle remains relatively unaffected [63]. As mentioned before in section 2.1, it should however be remarked that plasma bullets in He typically exhibit ring-shaped discharge structures that are different from those observed in N$_2$ [7, 43], and that in both former studies a ring electrode geometry was used instead of a single needle electrode. For streamer discharges in artificial air, Wormeester *et al* showed that, although the evolution times are different, the streamer radius and maximum electrical field remain practically the same while the preionization density was changed by two orders of magnitude in the absence of photoionization [60].

The effect of the characteristic width of the background ionization channel in our model was investigated by changing it to 0.125 mm and 0.375 mm. For the 0.125 mm case, the on-axis maximum field and the velocity were about 25% higher. In the 0.375 mm case, instabilities related to branching occurred, which resulted in fluctuating properties that are hard to evaluate. Since this behavior is not observed in the experiment it could indicate that the channel is at least narrower than 0.375 mm. On average, the on-axis

field in this case was about 15% lower than in the 0.25 mm case, and the velocity was about 25% lower.

Considering all this, the before mentioned factors together could perhaps explain a difference of 50% between the experimental and modeled field amplitudes presented in this work. On the other hand, with the same applied voltage a very similar propagation velocity is observed in the simulations and the experiments. While this agreement could indicate that the simulations represent the experimental discharge quite well, it must be remarked that the velocity not only depends strongly on the electric field around the streamer but also on its radius [59, 64].

From the experimental point of view, an error in the calibration could be a cause of error in the amplitudes. While care was taken to choose calibration electrodes shorter than twice the shortest Rayleigh length, deviations from the plane-wave approximation could result in an overestimation of the electric field integrals in the calibration. This would subsequently lead to an overestimation of the calibration constants and hence of the final electric field values. Moreover, potential calibration errors are also introduced by the spatial drift of the laser beams between the calibration and the actual measurements. In addition, spatial drift of the laser beams during a series of measurements, as well as the sampling of 400 shots, could contribute to broadening of the measured distribution. Lastly, the choice of fit function also has some influence on the final electric field profile, particularly on the center values. Taking these things into account, the error in the experimentally found values is also estimated up to several tens of percent. Given these uncertainties, the differences between the electric field profiles from the measurements and the model are reasonable.

3.2.2. Temporal scans The temporal scans are also made at a fixed distance from the nozzle $z_0 = 1$ mm at three fixed y-positions to see the evolution of the electric field at these points as the bullet propagates. The three y-positions are 465, 965 and 1465 µm from the jet axis and are illustrated by the red points in figure 11b. Comparing with figure 2, it can be seen that the outer two y-positions are situated well outside the region of optical emission. The results of the temporal scans are shown in figure 16. Since these measurement are conducted at only three fixed y-positions, an inversion cannot be performed. Instead, the square root of the ratio of measured intensities, which is proportional to the electric field integral, is qualitatively compared to the model at these positions. To get the equivalent data from the model, the electric field is this time projected onto a cartesian grid, spatially and temporally convolved with the laser beam profiles, and integrated along the x-axis. Since the measured temporal profiles are obtained by changing the timing between the discharge and the lasers, it should be realized that the interval between data points does not indicate the actual temporal resolution of the measurement system, which is limited by the laser pulse duration as discussed before.

In figure 16a the measured evolution of the z-component of the field is shown. The axial fields increase until the bullet reaches the position of the laser at about 20 ns, and
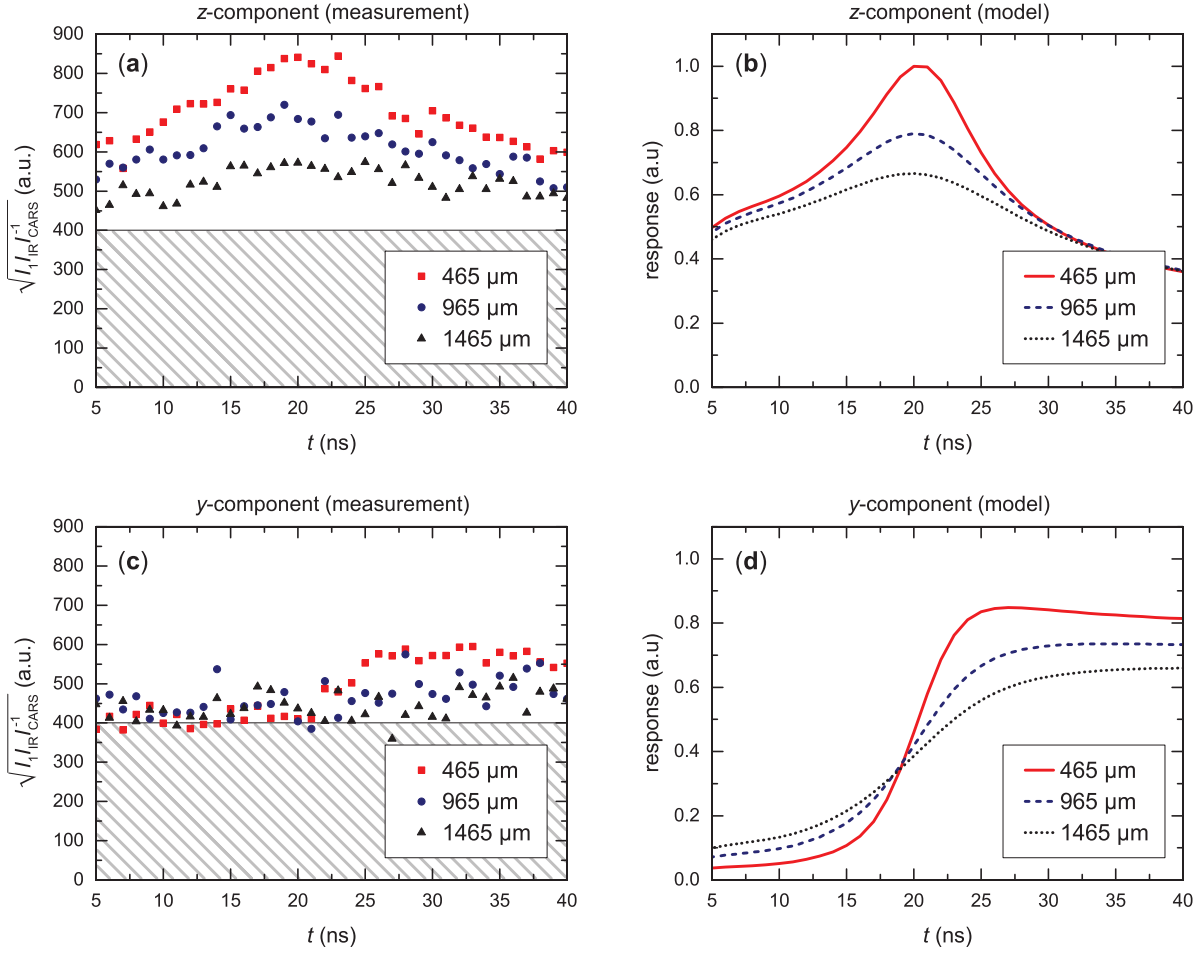
Figure 16. Temporal profiles of the integrated z-component of the electric field obtained from the experiment (a) and the model (after convolution and integration) (b), and of the integrated y-component of the electric field obtained from the experiment (c) and the model (after convolution and integration) (d). The hatched areas in (a) and (c) indicate the region that is below the measurement threshold.

then decrease again as the bullet propagates past the lasers. As expected, the axial component is largest at the position closest to the jet axis and decreases further away. The evolution of the electric fields in the model shows comparable behavior in figure 16b. The y-component measurements in figure 16c are all around the threshold value before 20 ns. This is in line with the spatial scan in the previous subsection, which was performed right before the bullet reaches the laser position and where no significant y-component could be detected. Looking at the results from the model in figure 16d indeed shows that the radial fields before 20 ns are lower than after 20 ns at all three positions. For the profiles at 465 µm from the jet axis, a similar shape can be recognized after 20 ns. This increase of the y-component of the electric field when the bullet propagates past the laser beam position around 20 ns results from the net space charge layer that surrounds and screens the inner streamer channel, and produces a radial electric field outside the streamer channel. For the two profiles further from the axis this is less obvious in the

measurements because they remain close to the threshold. However, the values of the points measured after 20 ns at 965 µm are on average larger than the points measured at 1465 µm, which is in agreement with the model. Similar behavior of the radial field component was also observed with an electro-optic probe placed outside the dielectric tube for plasma bullets in He [21]. Finally, both the experiments and the model show that the maximum value of the y-component is lower than the maximum value of the z-component.

4. Conclusions and outlook

In this work the electric field four-wave mixing technique is applied to plasma bullets in N$_2$. It is demonstrated that it is feasible to obtain local values of a non-uniform electric field distribution by extending this technique with an inversion method. Furthermore, a calibration procedure using electrodes different from the discharge geometry is demonstrated. A radial profile is obtained for the axial component of the electric field in front of the plasma bullet with a peak value of about 12–18 kV/mm and a FWHM of 750–900 µm. While the limited temporal resolution of the system leads to an underestimation of the true peak value, the found value is in the expected range for streamer discharges from literature. The streamer model predicts electric field values about a factor two lower than the experiment as well as a faster radial decay. Nevertheless, these differences are reasonable considering the used approximations and the experimental uncertainties. In addition, three temporal profiles were obtained for fixed points in space as the bullet propagates. Here it is found that the axial component increases as the bullet travels towards the measurement position and then decreases again. The radial component of the electric field only reaches values above the measurement threshold after the front of the bullet has passed the measurement position. Qualitatively similar features are observed in the model.

   To further improve the measurements in the future, most importantly the temporal resolution of the setup needs to be increased. One way to achieve this is using a picosecond laser system, such as used by Goldberg *et al* [34, 35], instead of a nanosecond laser system. Another option, which is currently being pursued, is using a faster and more sensitive detection system to temporally resolve the measurements within the laser pulse. In addition, the effect of the size of the calibration electrodes, and the resulting calibration electric field, relative to the Rayleigh length of the focused laser beams should be investigated to establish the accuracy of the calibration constant and hence of the electric field amplitudes. For a better comparison to the model, most importantly a reference potential should be defined in the experiment to provide a proper boundary condition. This can for example be achieved by placing a grounded cylindrical vessel around the plasma source. The uncertainty in the current implementation of the memory effect as a gaussian channel of background ionization could be avoided by extending the model to multiple consecutive discharges and including the gas flow. Furthermore, calculating radiative decay of excited species in the model would allow a

direct comparison of the model to the ICCD camera images and the corresponding radii. Together, this will make it possible to obtain fully spatially and temporally resolved electric field profiles of plasma bullets in N$_2$.

Acknowledgments

References

[1] Lu X, Laroussi M and Puech V 2012 *Plasma Sources Sci. Technol.* **21** 034005
[2] Winter J, Brandenburg R and Weltmann K D 2015 *Plasma Sources Sci. Technol.* **24** 064001
[3] Brandenburg R 2017 *Plasma Sources Sci. Technol.* **26** 053001
[4] Teschke M, Kedzierski J, Finantu-Dinu E, Korzec D and Engemann J 2005 *IEEE Trans. Plasma Sci.* **33** 310–311
[5] Lu X and Laroussi M 2006 *J. Appl. Phys.* **100** 063302
[6] Hofmann S, Sobota A and Bruggeman P 2012 *IEEE Trans. Plasma Sci.* **40** 2888–2899
[7] Lu X, Naidis G V, Laroussi M and Ostrikov K 2014 *Phys. Rep.* **540** 123–166
[8] Lacoste D a, Bourdon A, Kuribara K, Urabe K, Stauss S and Terashima K 2014 *Plasma Sources Sci. Technol.* **23** 062006
[9] Wujec T, Janus H W and Jele ski W 2003 *J. Phys. D. Appl. Phys.* **36** 868–877
[10] Wang Q, Koleva I, Donnelly V M and Economou D J 2005 *J. Phys. D. Appl. Phys.* **38** 1690–1697
[11] Obradovic B M, Ivkovic S S and Kuraica M M 2008 *Appl. Phys. Lett.* **92** 191501
[12] Ivković S S, Obradović B M and Kuraica M M 2012 *J. Phys. D. Appl. Phys.* **45** 275204
[13] Olszewski P, Wagenaars E, McKay K, Bradley J W and Walsh J L 2014 *Plasma Sources Sci. Technol.* **23** 015010
[14] Sretenović G B, Krstić I B, Kovačević V V, Obradović B M and Kuraica M M 2014 *J. Phys. D. Appl. Phys.* **47** 102001
[15] Sobota A, Guaitella O, Sretenović G B, Krstić I B, Kovačević V V, Obrusník A, Nguyen Y N, Zajíčková L, Obradović B M and Kuraica M M 2016 *Plasma Sources Sci. Technol.* **25** 065026
[16] Ivković S S, Sretenović G B, Obradović B M, Cvetanović N and Kuraica M M 2014 *J. Phys. D. Appl. Phys.* **47** 055204
[17] Kozlov K V, Wagner H E, Brandenburg R and Michel P 2001 *J. Phys. D. Appl. Phys.* **34** 3164–3176
[18] Kozlov K V and Wagner H E 2007 *Contrib. to Plasma Phys.* **47** 26–33
[19] Robert E, Darny T, Dozias S, Iseni S and Pouvesle J M 2015 *Phys. Plasmas* **22** 122007
[20] Bourdon A, Darny T, Pechereau F, Pouvesle J M, Viegas P, Iséni S and Robert E 2016 *Plasma Sources Sci. Technol.* **25** 035002
[21] Darny T, Pouvesle J M, Puech V, Douat C, Dozias S and Robert E 2017 *Plasma Sources Sci. Technol.* **26** 045008
[22] Sobota A, Guaitella O and Garcia-Caurel E 2013 *J. Phys. D. Appl. Phys.* **46** 372001
[23] Wild R, Gerling T, Bussiahn R, Weltmann K D and Stollenwerk L 2014 *J. Phys. D. Appl. Phys.* **47** 042001
[24] Slikboer E, Guaitella O and Sobota A 2016 *Plasma Sources Sci. Technol.* **25** 03LT04
[25] Slikboer E, Garcia-Caurel E, Guaitella O and Sobota A 2017 *Plasma Sources Sci. Technol.* **26** 035002
[26] Kong M G, Kroesen G, Morfill G, Nosenko T, Shimizu T, van Dijk J and Zimmermann J L 2009 *New J. Phys.* **11** 115012

[27] Gavrilenko V P, Kupryanova E B, Okolokulak V N, Ochkin V N, Savinov S Y, Tskha S N and Yarashev A N 1992 *JETP Lett.* **56** 1–4

[28] Evsin O a, Kupryanova E B, Ochkin V N, Savinov S Y and Tskhai S N 1995 *Quantum Electron.* **25** 278–282

[29] Akimov D A, Zheltikov A M, Koroteev N I and Naumov A N 1999 *Jetp Lett.* **70** 375–379

[30] Tskhai S N, Akimov D A, Mitko S V, Ochkin V N, Serdyuchenko A Y, Sidorov-Biryukov D A, Sinyaev D V and Zheltikov A M 2001 *J. Raman Spectrosc.* **32** 177–181

[31] Ito T, Kobayashi K, Czarnetzki U and Hamaguchi S 2010 *J. Phys. D. Appl. Phys.* **43** 062001

[32] Müller S, Luggenhölscher D and Czarnetzki U 2011 *J. Phys. D. Appl. Phys.* **44** 165202

[33] Yatom S, Tskhai S and Krasik Y E 2013 *Phys. Rev. Lett.* **111** 255001

[34] Goldberg B M, Böhm P S, Czarnetzki U, Adamovich I V and Lempert W R 2015 *Plasma Sources Sci. Technol.* **24** 055017

[35] Goldberg B M, Shkurenkov I, O'Byrne S, Adamovich I V and Lempert W R 2015 *Plasma Sources Sci. Technol.* **24** 035010

[36] Böhm P, Kettlitz M, Brandenburg R, Höft H and Czarnetzki U 2016 *Plasma Sources Sci. Technol.* **25** 054002

[37] Goldberg B M, Shkurenkov I, Adamovich I V and Lempert W R 2016 *Plasma Sources Sci. Technol.* **25** 045008

[38] Ito T, Kobayashi K, Müller S, Luggenhölscher D, Czarnetzki U and Hamaguchi S 2009 *J. Phys. D. Appl. Phys.* **42** 092003

[39] Lempert W R, Kearney S P and Barnat E V 2011 *Appl. Opt.* **50** 5688

[40] Ito T, Kanazawa T and Hamaguchi S 2011 *Phys. Rev. Lett.* **107** 1–4

[41] Simeni Simeni M, Goldberg B M, Zhang C, Frederickson K, Lempert W R and Adamovich I V 2017 *J. Phys. D. Appl. Phys.* **50** 184002

[42] Hübner S, Hofmann S, van Veldhuizen E M and Bruggeman P J 2013 *Plasma Sources Sci. Technol.* **22** 065011

[43] Naidis G V 2011 *J. Phys. D. Appl. Phys.* **44** 215203

[44] Ochkin V N 2009 *Spectroscopy of Low Temperature Plasma* (Weinheim, Germany: Wiley-VCH Verlag GmbH & Co. KGaA) ISBN 9783527627509

[45] Lempert W R and Adamovich I V 2014 *J. Phys. D. Appl. Phys.* **47** 433001

[46] Boyd R W 2008 *Nonlinear optics* 3rd ed (New York: Academic Press) ISBN 9780123694706

[47] Gavrilenko V P, Ochkin V N and Tskhai S N 2002 *Proc. SPIE* **4460** 207–229

[48] Griem H R 1997 *Principles of Plasma Spectroscopy* Cambridge Monographs on Plasma Physics (Cambridge University Press)

[49] Pretzler G 1991 *Zeitschrift für Naturforsch. A* **46a** 639–641

[50] Dribinski V, Ossadtchi A, Mandelshtam V A and Reisler H 2002 *Rev. Sci. Instrum.* **73** 2634

[51] Luque A and Ebert U 2012 *J. Comput. Phys.* **231** 904–918

[52] Phelps database, retrieved April 3 2017 URL `www.lxcat.net`

[53] Hagelaar G J M and Pitchford L C 2005 *Plasma Sources Sci. Technol.* **14** 722–733

[54] Teunissen J and Ebert U 2017 *Submitt. to Comput. Phys. Commun.*

[55] Nijdam S, Teunissen J, Takahashi E and Ebert U 2016 *Plasma Sources Sci. Technol.* **25** 44001

[56] Nijdam S, Takahashi E, Markosyan A H and Ebert U 2014 *Plasma Sources Sci. Technol.* **23** 025008

[57] Pancheshnyi S, Starikovskaia S and Starikovskii A 2000 *Chem. Phys.* **262** 349–357

[58] Shcherbakov Y V and Sigmond R S 2007 *J. Phys. D. Appl. Phys.* **40** 460–473

[59] Naidis G V 2009 *Phys. Rev. E* **79** 057401

[60] Wormeester G, Pancheshnyi S, Luque A, Nijdam S and Ebert U 2010 *J. Phys. D. Appl. Phys.* **43** 505201

[61] Bonaventura Z, Bourdon A, Celestin S and Pasko V P 2011 *Plasma Sources Sci. Technol.* **20** 035012

[62] Boeuf J P, Yang L L and Pitchford L C 2013 *J. Phys. D. Appl. Phys.* **46** 015201

[63] Breden D, Miki K and Raja L L 2012 *Plasma Sources Sci. Technol.* **21** 034011

[64] Sretenović G B, Krstić I B, Kovačević V V, Obradović B M and Kuraica M M 2014 *J. Phys. D.*

Appl. Phys. **47** 355201